

Noise radiated by low-Reynolds number flows past a hemisphere at $Ma = 0.3$

Hua-Dong Yao,^{a)} Lars Davidson, and Lars-Erik Eriksson

Department of Applied Mechanics, Chalmers University of Technology, Gothenburg, Sweden

(Received 15 March 2017; accepted 5 July 2017; published online 20 July 2017)

Flows past a hemisphere and their noise generation are investigated at the Reynolds numbers (Re) of 1000 and 5000. The Mach number is 0.3. The computational method of the flows is large eddy simulation. The noise is computed using the Ffowcs Williams and Hawkins Formulation 1C (FIC). An integral surface with an open end is defined for the FIC. The end surface is removed to reduce the numerical contamination that is introduced by vortices passing this surface. However, the contamination cannot be completely reduced since a discontinuity of the flow quantities still exists at the open surface boundary. This problem is solved using a surface correction method, in which a buffer zone is set up at the end of the integral surface. The transformation of flow structures due to Re is explored. Large coherent structures are observable at low Re , whereas they diminish at high Re . A large amount of small-scale turbulent vortices occur in the latter case. It is found that these characteristics of the flows have an important influence on the noise generation in regard to the noise spectra. In the flows studied in this work, the fluctuating pressure on the walls is a negligible noise contributor as compared with the wake. *Published by AIP Publishing.* [<http://dx.doi.org/10.1063/1.4994592>]

I. INTRODUCTION

Flows past bluff bodies are widely studied due to the generation of dynamic surface forces and noise. A hemisphere is a classic blunt body that has received interest in the vehicle industry as a simplification of side-view mirrors. In addition, as compared with geometries with long spanwise lengths (e.g., a cylinder or a flat plate), the hemisphere excludes approximations in the spanwise direction. This feature is beneficial in the validation of a numerical methodology for noise computation.

The hemisphere flows at low Re up to 300 were studied using direct numerical simulations (DNSs).¹ Unsteady planar-symmetric coherent structures are detected in the wakes for $Re > 210$. However, there are few studies in the literature on the turbulence and noise generation induced by this type of bluff body.

The computation of noise is difficult since acoustic waves have low energy and propagate with low dissipation. This difficulty can be resolved using the acoustic analogy proposed by Lighthill.^{2,3} The method was further developed to include stationary walls by Curle⁴ and moving walls by Ffowcs Williams and Hawkins (FW-H).⁵ The initial form of the Ffowcs Williams and Hawkins (FW-H) equation is categorized as Formulation 0 (F0). Some improvements for F0 were implemented in Formulations 1 (F1) and 1A (F1A).^{6,7} However, these formulations do not take into account the convection of the mean flow that deflects the wave propagation. The convection can be implicitly considered by moving microphones,⁸ but this treatment brings about high computational costs. An alternative is Formulation 1C (FIC),^{9,10}

which explicitly includes the convection to save computational resources.

In applications of the FW-H formulations, a general question is how to dispose of the end of a permeable integral surface. The surface is required to enclose flow structures that generate the noise. However, this requirement could not be well satisfied in the situation that a wake exists far downstream. If the surface is not extended sufficiently downstream, numerical contamination will arise due to the flow quantities truncated on the end part of the surface, which is normal to the streamwise direction. A method of reducing the contamination is to damp quadrupole sources.^{11,12} Another approach is the correction of the boundary fluxes with a precondition that the convection is frozen in time.¹³ This approach is improved by freezing the convection in the frequency domain.¹⁴ Removing the end part of the surface is also a solution for disregarding the truncated sources.^{15,16} However, this method still brings the contamination due to the discontinuity of the flow quantities at the surface boundary. A correction method was proposed for the Kirchhoff formulation with an open surface,¹⁷ but this formulation excludes the nonlinear terms on the surface and is different from the FW-H formulations.

This work aims to investigate the turbulence and noise induced by the hemisphere. The influence of Re on the flow structures in the wakes will be explored. The dependence of the noise generation on the flow structures will be clarified. A simple surface correction method for the FIC will be adopted and validated.

II. PERMEABLE SURFACE CORRECTION APPROACH

As the FIC has been well documented in the literature,^{9,10} the details on the derivation of this formulation are presented in the [Appendix](#). A permeable surface used in the FIC can be split

^{a)}Electronic mail: huadong@chalmers.se.

into two parts: one resolved in the computation and the other unresolved. The FIC contains a set of integrals contributing to the far-field noise. A general form of the integrals can be defined as

$$4\pi p'_i = \mathcal{L} \left\{ \int_{f=0|rs} [s_i]_{ret} dS + \int_{f=0|urs} [s_i]_{ret} dS \right\}, \quad (1)$$

where subscript “rs” means the resolved part, subscript “urs” means the unresolved part, and subscript “ret” denotes the term at the retarded time. The control surface of the integrals is defined by $f=0$. The term s_i is the general form representing the sources contributing to the generation of the noise component p'_i . The operator \mathcal{L} represents the general form of the derivatives taken for the integrals. For example, in the first integral of the thickness noise p'_T [see Eq. (A7a) in the Appendix], $\mathcal{L} = \partial/\partial t$ and $s_i = Q_j n_j / [R^* (1 - M_R)]$.

Artificial noise is generated owing to the discontinuity of the source terms at the border line of the resolved surface part, which connects to the unresolved part. An idea for reducing the discontinuity is to gradually damp the sources to a negligible level at the border line.^{17,24–26} To realize this idea, a buffer zone that brings in the damping effect is introduced at the end of the resolved surface part. A sketch of the idea is illustrated in Fig. 1. The noise from the resolved surface is therefore given by¹⁷

$$\begin{aligned} \mathcal{L} \int_{f=0|rs} [s_{sum}]_{ret} dS &\approx \mathcal{L} \int_{f=0|norm} [s_{sum}]_{ret} dS \\ &+ \mathcal{L} \int_{f=0|buff} [s_{sum}]_{ret} (1 - w_d) \\ &\times (\vec{y}, \vec{r}_{min}, \vec{r}_{max}) dS, \end{aligned} \quad (2)$$

where subscript “norm” denotes the normal surface part without the damping and subscript “buff” denotes the buffer zone. $w_d(\vec{y}, \vec{r}_{min}, \vec{r}_{max})$ is the damping factor that can be defined with a bell-shaped window function or a smooth exponential function. \vec{r}_{min} is the starting position of the buffer zone and \vec{r}_{max} is the position of the border line.

The correction method presented above can easily be implemented in either a computational fluid dynamics (CFD)

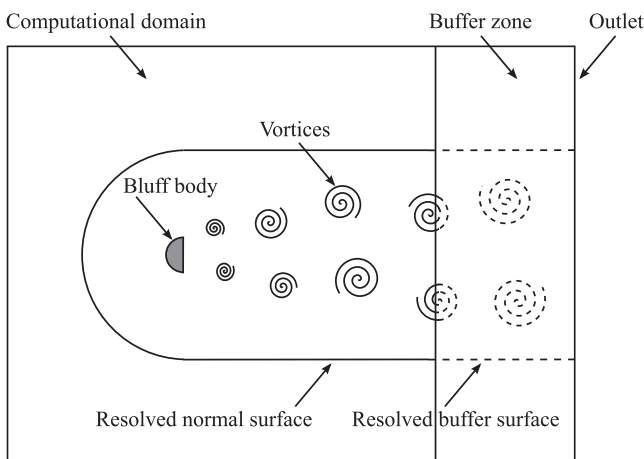


FIG. 1. A sketch of the normal and buffer parts of a resolved permeable integral surface.

solver or the post-processing of the noise sources. In this work, since a buffer zone is already created for the flow computation, it is convenient to reuse this buffer zone for the noise computation.

III. GOVERNING EQUATIONS OF LARGE EDDY SIMULATION (LES)

For an ideal gas, the governing equations of the LES in consideration of the compressibility are

$$\frac{\partial Q}{\partial t} + \frac{\partial F_j}{\partial x_j} = 0, \quad (3)$$

where

$$Q = \begin{bmatrix} \bar{\rho} \\ \bar{\rho} \tilde{u}_i \\ \bar{\rho} \tilde{e}_0 \end{bmatrix}, \quad (4)$$

$$F_j = \begin{bmatrix} \bar{\rho} \tilde{u}_j \\ \bar{\rho} \tilde{u}_i \tilde{u}_j + \bar{p} \delta_{ij} - \bar{\sigma}_{ij} - \tau_{ij} \\ \bar{\rho} \tilde{e}_0 \tilde{u}_j + \bar{p} \tilde{u}_j - C_p \left[\left(\frac{\mu}{\bar{p}} + \frac{\mu_t}{\bar{p}_t} \right) \frac{\partial \tilde{T}}{\partial x_j} \right] - \tilde{u}_i (\bar{\sigma}_{ij} + \tau_{ij}) \end{bmatrix}, \quad (5)$$

where the bar denotes the filtering with a convolution filter, and the tilde means the Favre filtering. In this work, a box filter is used as the convolution filter. The viscous stress tensor $\bar{\sigma}_{ij}$ is in the form of

$$\bar{\sigma}_{ij} = \mu \left(2\tilde{S}_{ij} - \frac{2}{3}\tilde{S}_{mn}\delta_{ij} \right). \quad (6)$$

The Smagorinsky model¹⁸ is used to model the sub-grid scale (SGS) viscous tensor τ_{ij} as

$$\tau_{ij} = \mu_t \left(2\tilde{S}_{ij} - \frac{2}{3}\tilde{S}_{mn}\delta_{ij} \right) - \frac{2}{3}\bar{\rho} k_{SGS} \delta_{ij}, \quad (7)$$

where k_{SGS} is the SGS kinetic energy given by

$$k^{SGS} = C_I \Delta^2 \tilde{S}_{mn} \tilde{S}_{mn}. \quad (8)$$

μ_t is the SGS dynamic viscosity defined as

$$\mu_t = C_R \bar{\rho} \Delta^2 \sqrt{\tilde{S}_{mn} \tilde{S}_{mn}}. \quad (9)$$

The Favre-filtered strain rate tensor \tilde{S}_{ij} is represented as

$$\tilde{S}_{ij} = \frac{1}{2} \left(\frac{\partial \tilde{u}_i}{\partial x_j} + \frac{\partial \tilde{u}_j}{\partial x_i} \right). \quad (10)$$

The filter width in Eqs. (8) and (9) is the minimum length of a mesh cell, $\Delta = \min(\Delta_1, \Delta_2, \Delta_3)$. The constants are set as

$$C_R = 0.012, \quad C_I = 0.0066. \quad (11)$$

IV. COMPUTATIONAL METHOD

A. Numerical discretization

The governing equations are solved by means of a cell-centred finite volume method. Discretization of the convective fluxes is performed using a low dissipation 3rd-order upwind scheme, which consists of the centred and upwind-biased components.^{19–21} The scheme coefficients on a cell face are determined by solving 3rd-order polynomial equations, which are

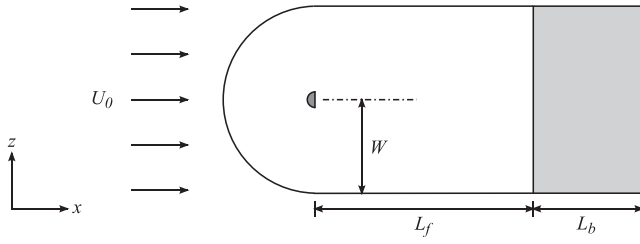


FIG. 2. A sketch of the computational domain in the cut plane of $y = 0$. The buffer zone is colored gray. The domain is axisymmetric. The parameters W , L_f , and L_b are referred in Table I.

formulated for the normal flux variations. The diffusive fluxes are discretized with a 2nd-order central difference scheme. The time marching algorithm utilizes the 2nd-order three-stage explicit Runge-Kutta approach. The solver comes from the in-house code called G3D.²⁰

B. Computational settings

The diameter of the hemisphere, D , is 1 m. In the free stream, the streamwise velocity U_0 is 100 m/s in the cases at different Reynolds numbers. The Mach number $M a_0$ is set as 0.294. The density ρ_0 is specified as 1.225 kg/m^3 . The heat capacity ratio γ_0 is 1.4. The Prandtl number Pr_0 is 0.72. The Reynolds numbers Re are 1000 and 5000 in terms of D and the free-stream conditions. Re are changed by adapting the dynamic viscosity μ_0 .

The computational domain comprises a hemispherical part and a cylindrical part. The cut plane of $y = 0$ in the domain is sketched in Fig. 2. The origin of the Cartesian coordinate system is located at the center of the back face of the hemisphere. The geometry is designed to reduce the incidence angles of acoustic waves propagating onto the boundaries. Large incidence angles can lead to numerical reflection.²² In

the cylindrical part, a buffer zone is constructed downstream to damp the vortices, which pass the outlet, and the artificial acoustic waves, which are generated due to the vortices cut off at the outlet.

To investigate the influence of the domain size on the computation, two domains with different dimension parameters are constructed. These parameters are listed in Table I. W is the domain radius, as shown in Fig. 2. L_f is the length from the back face of the hemisphere to the buffer zone. L_b is the length of the buffer zone. Hereafter, the lengths are scaled in terms of D . The time is scaled with the characteristic time $T = D/U_0$. The Strouhal number is defined as $St = fD/U_0$.

The damping terms in the buffer zone are specified as

$$Q_{damp} = w_d (Q - \langle Q \rangle) \quad (12)$$

with the damping factor

$$w_d = 1 - e^{-\varepsilon(x-x_{min})/U_0}, \quad (13)$$

where Q represents the quantities in Eq. (4) and $\langle Q \rangle$ denotes the time-average values of Q . x_{min} and x_{max} are the beginning and ending positions of the damping zone, respectively. ε is a constant. It is adjusted to 0.177 in this work.

The characteristic absorbing boundary condition²² is imposed on the domain boundaries, where the total pressure and enthalpy are specified. The adiabatic no-slip boundary condition is used on the surfaces of the hemisphere.

The computational meshes are structured. The mesh quality is examined with a coarse mesh in a small domain (mesh 1) and a refined mesh in a large domain (mesh 2). The computational time intervals set for the two meshes are different in order to satisfy the requirement of the Courant-Friedrichs-Lewy (CFL) condition. The meshes are used for both the cases. The mesh parameters and time intervals are presented in Table I. The surface mesh of mesh 2 is shown in Fig. 3.

TABLE I. The computational settings.

	W	L_f	L_b	n_c^a	Δh_1^b	$\Delta_1 _{x=5}^c$	$\Delta_1 _{x=10}^c$	$\Delta_1 _{x=20}^c$	$\Delta_1 _{x_{max}}^c$	n_{tot}^d	Δt^e
Mesh 1	12.5	20	10	164	0.002	0.086	0.173	0.269	0.44	1.39×10^7	5×10^{-4}
Mesh 2	22.5	25	30	188	0.001	0.045	0.086	0.2	2	2.68×10^7	1×10^{-4}

^aThe number of the nodes circumferentially surrounding the hemisphere.

^bThe first cell heights near the walls.

^cThe streamwise cell sizes along the axisymmetric line.

^dThe total number of the nodes.

^eThe dimensionless time interval.

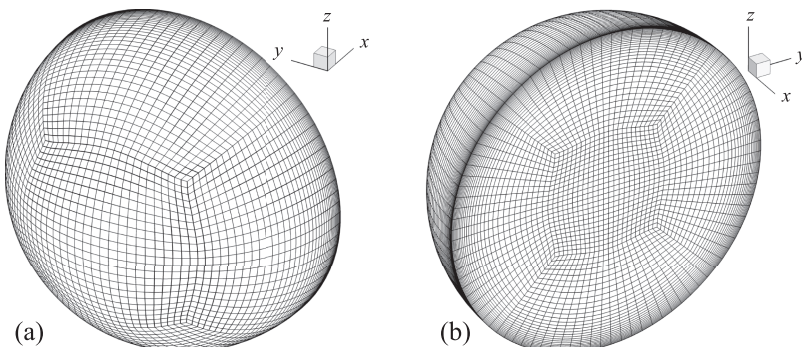


FIG. 3. The surface mesh of mesh 2 drawn with every second grid line is viewed from (a) the upstream side and (b) the downstream side.

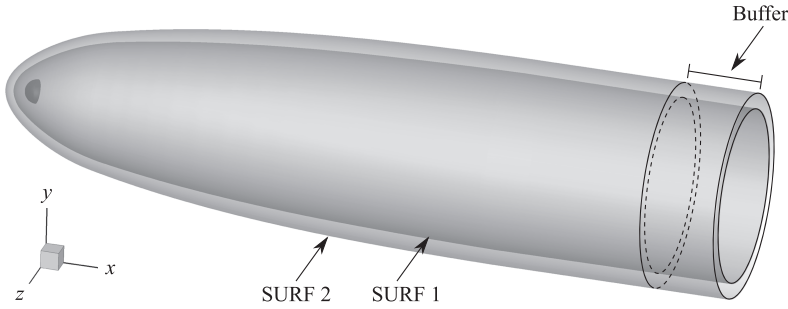


FIG. 4. The permeable control surfaces constructed for the noise computation.

The cells in mesh 2 are also refined in the wake region. Their streamwise lengths are half of those in mesh 1 for $x < 10$. The growth rates of the meshes are globally controlled below 1.05.

To inspect the convergence of the noise computation, two permeable surfaces, SURF 1 and SURF 2, are created. They are illustrated in Fig. 4. SURF 1 is constructed inside SURF 2. They are aligned with the grid lines of the meshes. The distance between the surfaces is approximately 1. The surfaces are open at the ends according to Eq. (1).

The buffer parts of the permeable surfaces are established by extending the surfaces into the buffer zone of the computational domain, where the damping is already imposed.

Therefore, w_d in Eq. (2) is formulated in the same way as Eq. (13).

V. VALIDATION OF COMPUTATIONAL SETTINGS

A. Mesh independence of flow computation

Snapshots of Δy^+ near the front face of the hemisphere in mesh 1 are illustrated in Fig. 5. The values of Δy^+ over the entire face are less than 1 in both the cases. Near the hemisphere edge where the flow separation could happen, the streamwise cell size, Δx , is 0.002 yielding $\Delta x^+ < 0.2$, and the circumferential cell size, Δz_c , is 0.019 yielding $\Delta z_c^+ < 1.9$. The

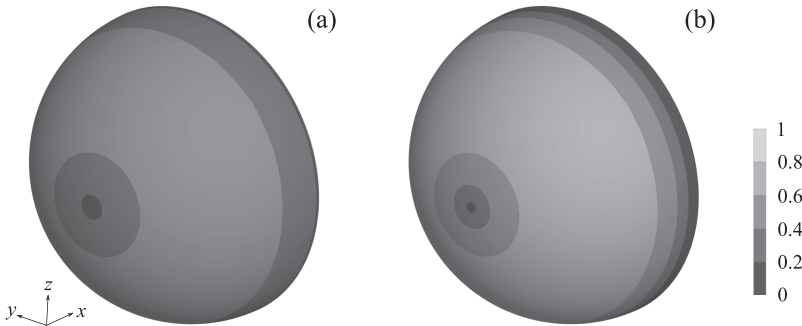


FIG. 5. Contours of instantaneous Δy^+ near the front face of the hemisphere in mesh 1 at (a) $Re = 1000$ and (b) $Re = 5000$.

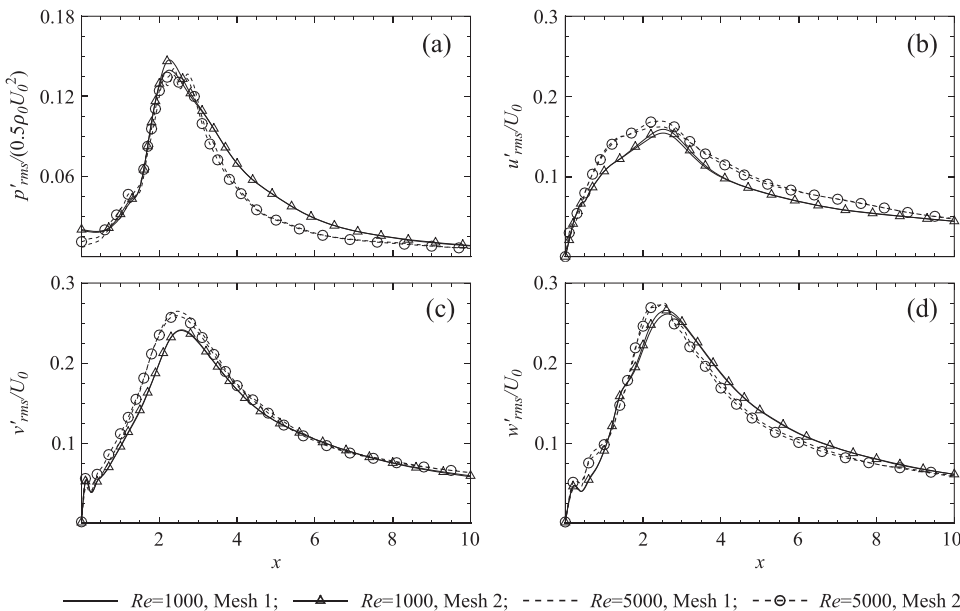


FIG. 6. The rms values of the pressure and velocity components along the axisymmetric line behind the hemisphere.

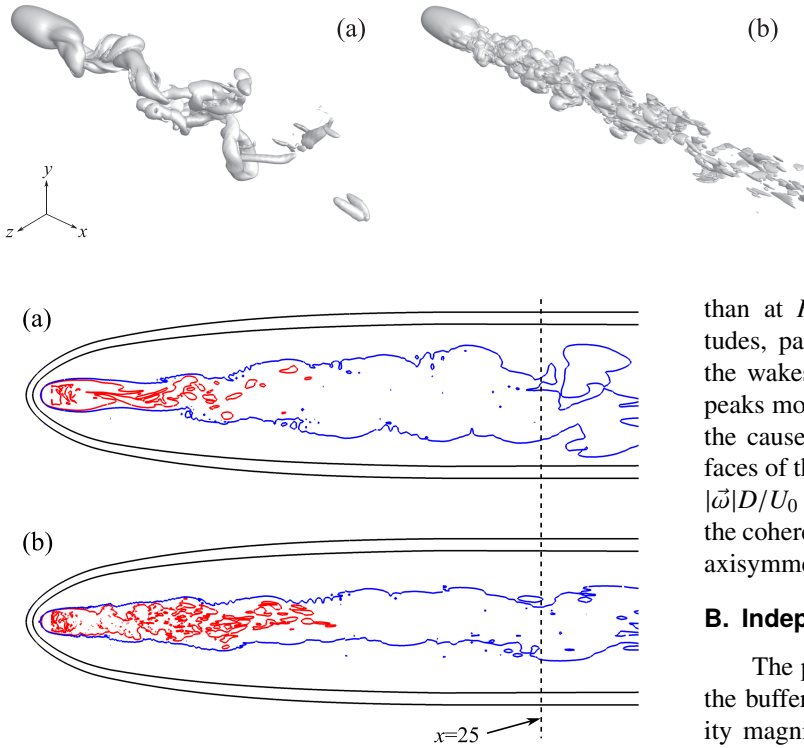


FIG. 7. Isosurfaces of the instantaneous vorticity magnitude, $|\vec{\omega}|D/U_0 = 0.8$, at (a) $Re = 1000$ and (b) $Re = 5000$.

FIG. 8. The permeable surfaces, SURF 1 and SURF 2, and the instantaneous dimensionless vorticity magnitudes, 0.02 (colored blue) and 1 (colored red), in the cut plane of $y = 0$ at (a) $Re = 1000$ and (b) $Re = 5000$.

mesh sizes of Δx^+ , Δy^+ , and Δz_c^+ satisfy the requirement of the wall-resolving LES to directly resolve the dynamics of the inner layer.²³

The root mean square (rms) values of the pressure and the velocity components along the axisymmetric line behind the hemisphere, computed with mesh 1 and mesh 2, are shown in Fig. 6. The physical time used in the calculation of the rms values is 414. The cell sizes in the wake from 0 to 10 in mesh 2 are half of those in mesh 1. The statistics of the velocity components and pressure fluctuations obtained based on the two meshes are nearly the same. This indicates that the flow computation is independent on the mesh quality and that the results converge. The turbulence in the wakes is therefore well resolved. For the sake of brevity, the flow quantities computed with mesh 2 are analyzed hereafter.

In addition, Fig. 6 shows that the rms values of the pressure at the two Re have similar magnitudes for $x < 3$. For $x > 3$, the pressure magnitudes at $Re = 5000$ decay more rapidly

than at $Re = 1000$. v_{rms} and w_{rms} have different magnitudes, particularly at low Re . The differences suggest that the wakes are not statistically axisymmetric. Moreover, the peaks move slightly upstream as Re increases. To investigate the cause of the differences between v_{rms} and w_{rms} , isosurfaces of the instantaneous dimensionless vorticity magnitude, $|\vec{\omega}|D/U_0 = 0.8$, are illustrated in Fig. 7. It is observed that the coherent structures in the wakes are not developed with an axisymmetric pattern.

B. Independence of permeable surface locations

The permeable surfaces, SURF 1 and SURF 2 including the buffer parts, and the instantaneous dimensionless vorticity magnitudes, 0.02 and 1, in the x - z plane are illustrated in Fig. 8. The regions with magnitudes above 0.02 are presumed to contain the energetic noise sources. The permeable surfaces are observed to enclose the regions completely. Furthermore, it is worth noting that the dimensionless vorticity magnitudes at the end of the normal part, $x = 25$, are smaller than 0.02.

The noise computed with the LES and F1C at the microphone position, $(x, y, z) = (8, 0, -10.5)$, is shown in Fig. 9. The results from SURF 1 and SURF 2 are consistent with those from the LES. Small discrepancies are observed since the noise is numerically dissipated due to the mesh cell expansion and numerical schemes. Both the surfaces are therefore feasible for the noise computation. Hereafter, the noise computed with SURF 2 including the buffer part is assessed.

C. Permeable surface correction

The noise at the microphone position, $(x, y, z) = (8, 0, -10.5)$, at $Re = 5000$ is shown in Fig. 10. The results are computed with SURF 2. The noise from the normal part is directly computed from the noise sources, which contain the physical components from low to high frequencies. Due to the discontinuity at the outflow boundary of the normal

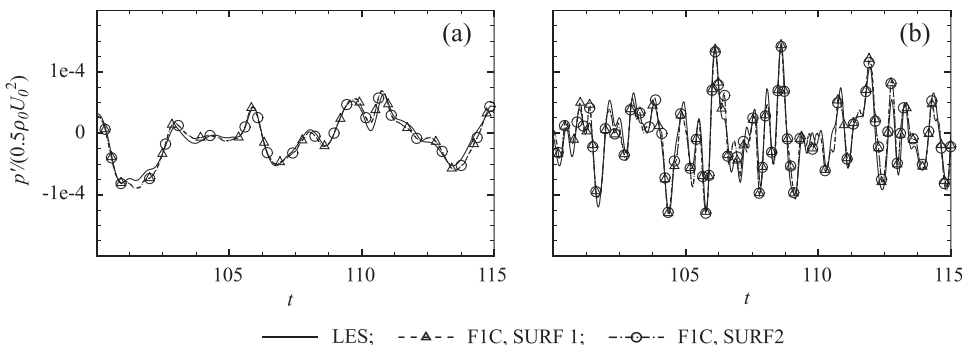


FIG. 9. The noise at the position, $(x, y, z) = (8, 0, -10.5)$, computed with the LES and F1C at (a) $Re = 1000$ and (b) $Re = 5000$. The curves obtained from SURF 1 coincide with those from SURF 2.

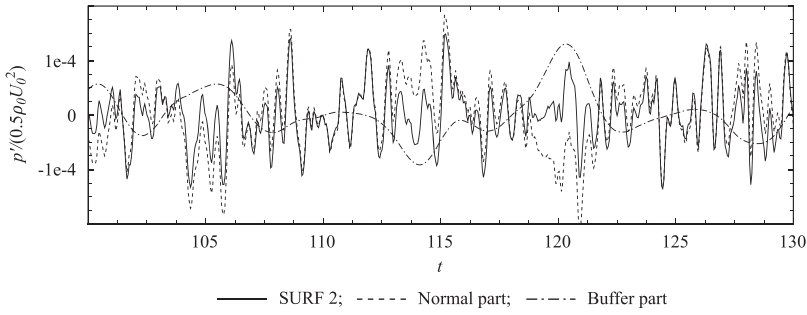


FIG. 10. The noise at the position, $(x, y, z) = (8, 0, -10.5)$, at $Re = 5000$. SURF 2 is used in the computation. The normal part of this surface excludes the damping. The buffer part is the region where the damping is imposed.

part, the noise would contain unphysical terms. To alleviate the unphysical terms, the sharp discontinuity is improved to a continuous zone with gradually damping effect by means of adding the buffer zone. Although the noise from the buffer part is used to reduce the unphysical terms, it is artificial since the flow in this region becomes smoothened. As shown in Fig. 9, the total noise predicted with the addition of the artificial buffer noise agrees well with the noise computed with the LES. On the other hand, Fig. 10 shows that the noise from the normal part is clearly different from the total noise. The contribution of the artificial buffer noise to the total noise is not negligible.

The noise is further studied in the spectrum measured in the sound pressure level (SPL) with the reference pressure $p_{ref} = 2 \times 10^{-5}$ Pa. The spectrum computed based on the discrete Fourier transformation (DFT) is smoothed with the one-third octave smoothing filter. The smoothed spectrum is given by

$$\hat{E}_s(f_i) = \frac{1}{n_b - n_a + 1} \sum_{i=n_a}^{n_b} |\hat{p}'(f_i)|^2, \quad (14)$$

$$n_a = \text{ceil}(2^{-1/6} f_i / \Delta f),$$

$$n_b = \text{floor}(2^{1/6} f_i / \Delta f),$$

where \hat{p}' is the pressure in the frequency domain, f_i denotes the i th frequency, and Δf is the frequency resolution of the spectrum. The operator *ceil* is used to find the

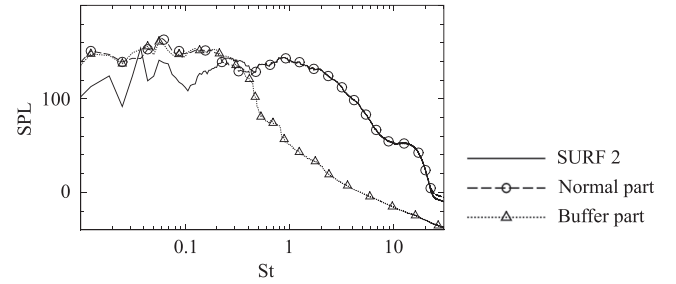


FIG. 11. The SPLs of the noise at the position, $(x, y, z) = (8, 0, -10.5)$, at $Re = 5000$. SURF 2 and its parts are used in the computation.

smallest integer that is above $2^{-1/6} f_i / \Delta f$ and *floor* to find the largest integer below $2^{1/6} f_i / \Delta f$. Hereafter, the one-third octave smoothing filter is employed to compute the SPL of the noise.

The SPLs of the total noise and its components at the position, $(x, y, z) = (8, 0, -10.5)$, at $Re = 5000$ are displayed in Fig. 11. SURF 2 and its parts are utilized in the computation. In the DFT, the bandwidth of the energy spectra is 1×10^4 Hz. The frequency resolution, Δf , is 0.625 Hz. The Hann window is used as the window function. The artificial buffer noise occurs at all frequencies, but its contribution to the total noise is negligible at frequencies above $St = 0.4$, where the noise from the normal part is dominant. At frequencies below $St = 0.4$, the noise from the normal part is noticeably overestimated by approximately 40 dB as compared with the total

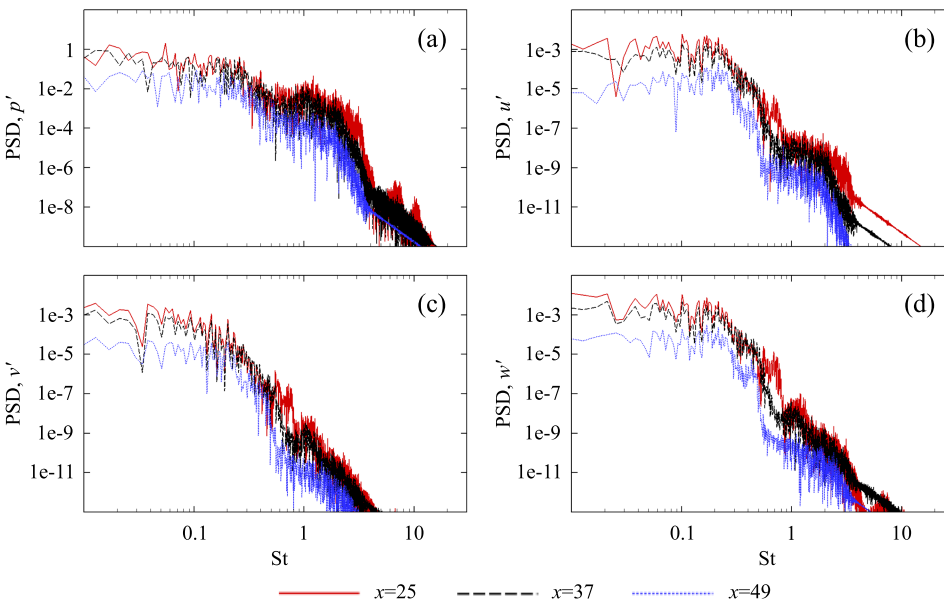


FIG. 12. The PSD of (a) p' , (b) u' , (c) v' , and (d) w' at $Re = 5000$ monitored at some positions in the buffer part of SURF 2. The monitor positions are located at $x = 25, 37,$ and 49 in the line defined by $y = 0$ and $z = -3.627$.

noise. For the sake of brevity, the case at $Re = 1000$ is not presented here.

The overestimation is compensated by the artificial buffer noise due to the improvement of the discontinuity of the noise sources at the outflow boundary of the normal part. This surface correction strategy has been investigated and suggested by Colonius *et al.*,²⁴ Freund *et al.*,¹⁷ Cheung and Lele,²⁵ and Bogey and Bailly.²⁶ In the present study, a question is why the compensation from the artificial buffer noise is significant in the low frequency range of $St < 0.4$. To answer this question, the power spectral density (PSD) of the pressure and velocity component fluctuations at $Re = 5000$ is monitored in the buffer part of SURF 2, as shown in Fig. 12. The monitors are located at different streamwise positions of $x = 25, 37,$ and 49 in the line defined by $y = 0$ and $z = -3.627$. At $x = 25$ where the buffer zone begins with the damping factor of zero, a common feature of the flow quantities is that the predominant energy appears at frequencies below $St = 0.4$. Other energy bulges occur for $0.6 < St < 1.2$, but their magnitudes are much lower. According to this common feature, the flow structures that enter in the buffer zone possess predominant energy at low frequencies. Moreover, the magnitudes of the spectra decrease with respect to the x coordinate along the downstream direction. The decreasing behavior is observed at all frequencies. The buffer zone therefore damps the spectra from low to high frequencies. Since the flow quantities forming the noise sources in the buffer part are energetic for $St < 0.4$, the noise produced by them is expected to be large at the same frequencies. This frequency range of the buffer noise is observed and supported in Fig. 11.

VI. RESULTS AND DISCUSSION

A. Flow field

The streamlines and contours of the time-average streamwise velocity, $\langle u \rangle$, near the edge of the hemisphere are

illustrated in Fig. 13. Here the angle brackets denote the time-average operator. The flows are laminar on the front face of the hemisphere. Flow separation occurs at $Re = 5000$. The adverse velocity emerges at $x = -0.022$.

The profiles of $\langle u \rangle / U_0$ along the z -axis at the streamwise positions of $y = 0$ and $x = -0.03, -0.02, -0.01,$ and 0 , which are near the edge of the hemisphere, are displayed in Fig. 14. The magnitudes at $Re = 1000$ increase slowly and are smaller than u_0 at $z = 0.55$. In contrast, the magnitudes grow rapidly at $Re = 5000$. They increase exponentially for $z < 0.525$ and gradually approach $1.1u_0$. Furthermore, negative values are observed between $x = -0.01$ and 0 for $z < 0.505$. This indicates the flow separation.

The drag coefficient C_{Dx} and the coefficients of the lift components, C_{Ly} and C_{Lz} , are shown in Fig. 15. The drag coefficient is defined as $C_{Dx} = D_x / (0.5\rho_0 U_0^2 S_A)$, where D_x is the drag and $S_A = 0.25\pi D^2$. The lift coefficients are defined in the same manner. These coefficients are statistically stationary in a recorded time of 230. The mean values of C_{Dx} are 0.414 at $Re = 1000$ and 0.385 at $Re = 5000$. The latter value is smaller than the former value since high Re causes more turbulent structures.

The history of C_{Ly} and C_{Lz} with respect to C_{Dx} in a recorded time of 230 is shown in Fig. 16. The two cases have turbulent traces. This indicates that the flows are turbulence. The values of C_{Dx} at low Re vary in a large range. It is found in Fig. 6 that p'_{rms} at $x = 0$, which is on the back face of the hemisphere, at high Re is smaller than that at low Re . Moreover, as shown in Fig. 7, the majority of turbulent structures that are observed in the wake at high Re have small scales, whereas coherent structures seen at low Re have large scales. The statistics of the surface pressure fluctuations on the back face are associated with the flow structures in the wake. We therefore believe that the larger variation range of C_{Dx} at low Re is associated with the coherent structures.

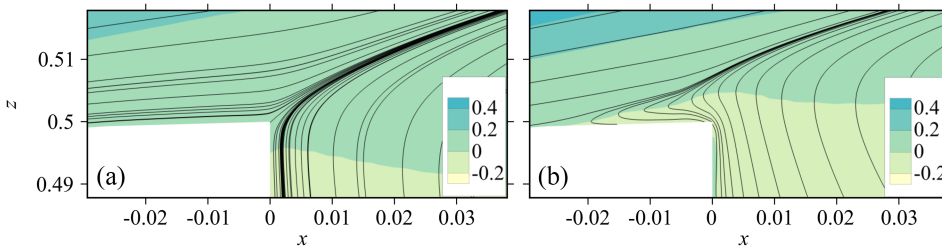


FIG. 13. Streamlines and contours of the time-average streamwise $\langle u \rangle / U_0$ near the edge of the hemisphere in the cut plane of $y = 0$ at (a) $Re = 1000$ and (b) $Re = 5000$.

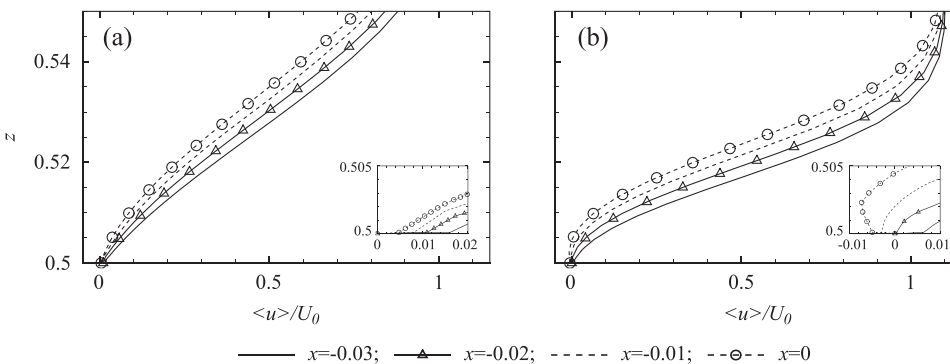


FIG. 14. Profiles of $\langle u \rangle / U_0$ at (a) $Re = 1000$ and (b) $Re = 5000$ along the z -axis at the positions of $y = 0$ and $x = -0.03, -0.02, -0.01,$ and 0 , which are near the edge of the hemisphere.

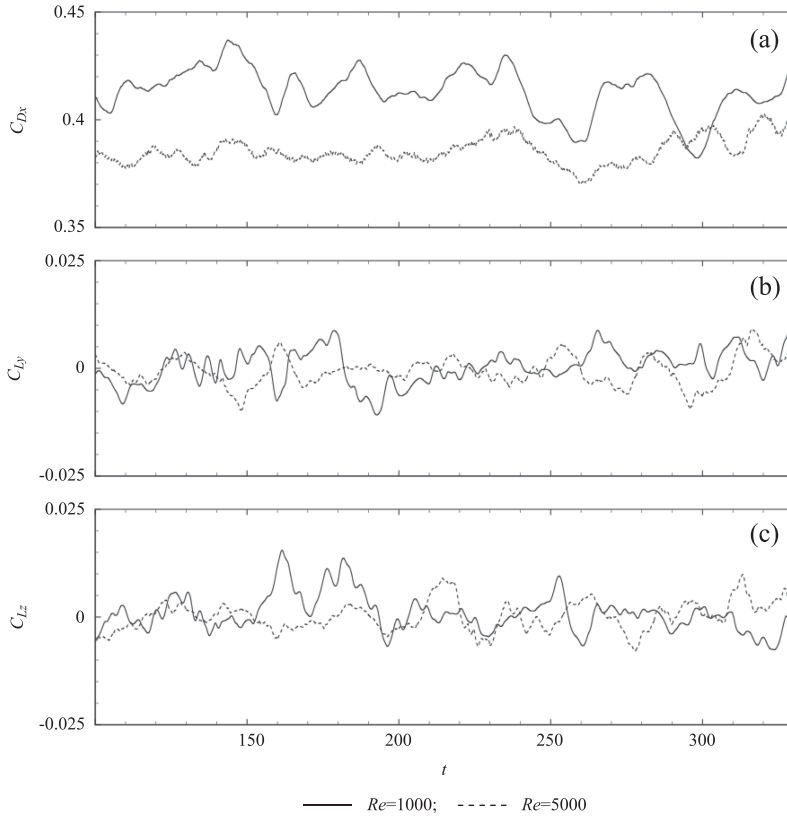


FIG. 15. (a) C_{Dx} , (b) C_{Ly} , and (c) C_{Lz} with respect to the dimensionless time t .

The power spectral density (PSD) of the drag D_x and the lift components, L_y and L_z , is shown in Fig. 17. The bandwidth of the spectra is 1×10^4 Hz. The frequency resolution is 0.507 Hz. The Hann window is used as the window function. The curve of L_y coincides with that of L_z in both the cases. At St below 0.2, the magnitudes of the forces at $Re = 1000$ are higher than those at $Re = 5000$. For $St > 0.2$, the magnitudes at low Re are smaller. This finding means that large scale coherent structures diminish as Re increases, whereas turbulent vortices become intensive. Two peaks are observed at $Re = 1000$. The Strouhal numbers, St , of the peaks are 4.15 and 8.61. At $Re = 5000$, a peak appears at $St = 11.48$. These frequencies are associated with the characteristic frequencies of the shedding that is detached from the edge of the hemisphere. Kim and Choi¹ found that the dominant frequency of the drag is twice the dominant frequency of the lift, which corresponds to St of 0.128, 0.127, and 0.135 at $Re = 200, 250,$ and 300 , respectively. To investigate this mechanism, the peak frequencies of the lift components in the range of 0.1–0.2 and the corresponding doubling frequencies of the drag are marked in

Fig. 17. Two obvious peaks of the lift coefficients are observed at St of 0.11 and 0.185 at $Re = 1000$. At the same St , the peaks of the lift coefficients are also noted at $Re = 5000$. At $St = 0.24$, energy bulges of the drag coefficient are seen in both the cases, while peaks at $St = 0.37$ are not noticeable.

Snapshots of the dimensionless vorticity component, $\omega_x D/U_0$, in the cut plane of $y = 0$ are shown in Fig. 18. The time interval between the snapshots is 1. The large scale coherent structures are observable in the wake at $Re = 1000$. A clear transverse expansion of them is detected. They flush downstream with a sweeping velocity of U_0 . At $Re = 5000$, the coherent structures are insignificant so that the wake expansion is not obvious. The small scale turbulent vortices become dominant in the wake. Their sweeping velocity is still U_0 .

Contours of u'_{rms} in the cut plane of $y = 0$ are shown in Fig. 19. As Re increases, the transverse width of the wake becomes narrow. The energy decays fast in the streamwise direction. Meanwhile, the high energy region moves upstream. The highest magnitudes are 0.261 at $Re = 5000$. It is slightly larger than 0.254 at $Re = 1000$. These phenomena are in line

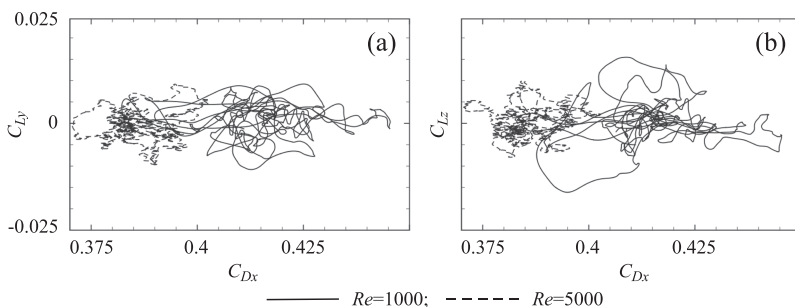


FIG. 16. History of the lift components (a) C_{Ly} and (b) C_{Lz} with respect to C_{Dx} in a dimensionless time of 230.

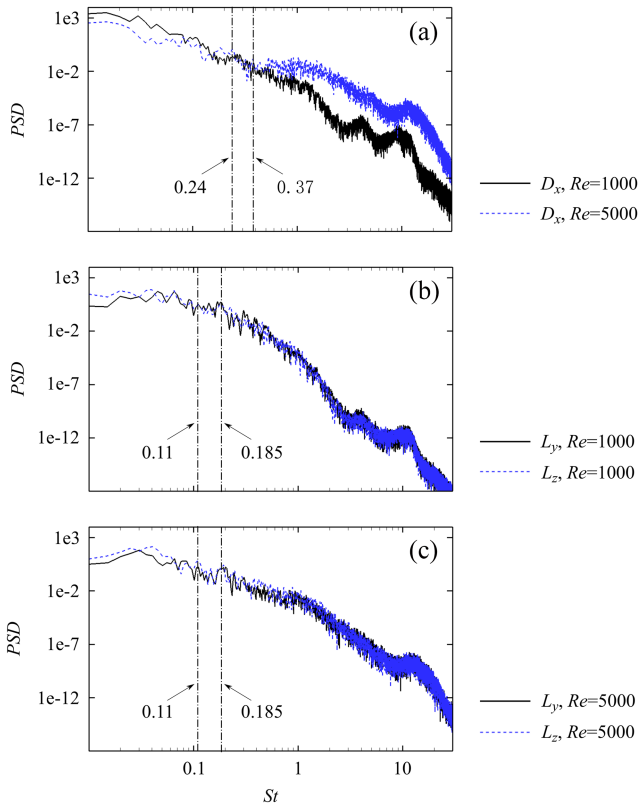


FIG. 17. The PSD of (a) the drag D_x at $Re = 1000$ and 5000 , (b) the lift components, L_y and L_z , at $Re = 1000$, and (c) L_y and L_z at $Re = 5000$. The dashed-dotted lines mark the peak frequencies in the lift components and the doubling lift-peak frequencies in the drag.

with the preceding finding that the small scale turbulent vortices increase at high Re , whereas the large scale coherent structures diminish.

B. Noise field

Snapshots of the pressure fluctuations are displayed in Fig. 20. At $Re = 1000$, the noise comes from the wake with relatively organized contours. The source regions join with the coherent structures. However, at high Re , the noise possesses an apparently turbulent feature and a variety of scales. An energetic source region is observed at the end of the recirculation bubble, where a strong convection occurs.

To investigate the noise in the far field, 36 microphones are evenly placed in a circle with a dimensionless radius of

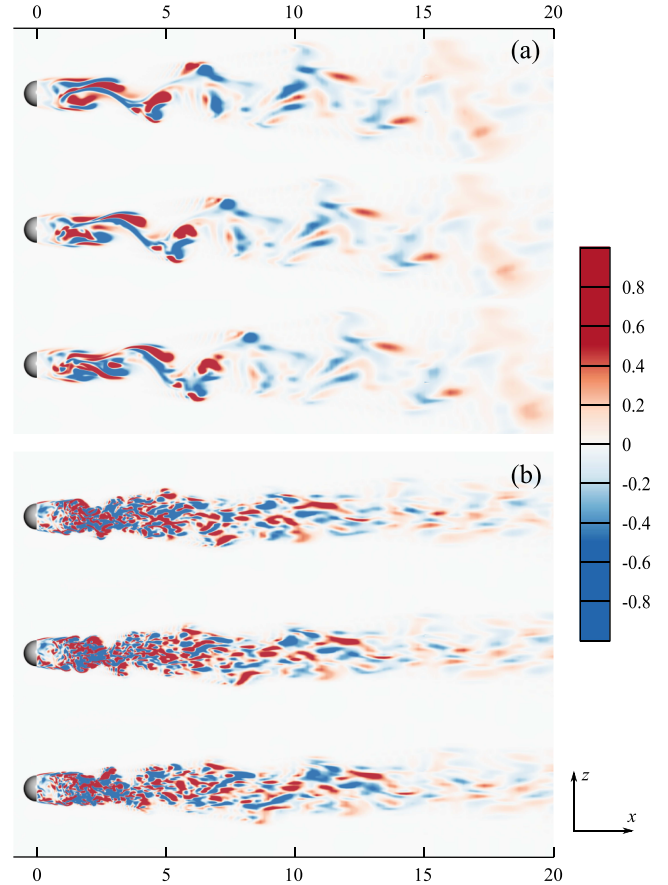


FIG. 18. Snapshots of the dimensionless vorticity component, $\omega_x D/U_0$, in the cut plane of $y = 0$ at (a) $Re = 1000$ and (b) $Re = 5000$. The time interval between the snapshots is 1.

50 in the plane of $y = 0$. The center of the circle is placed at the origin of the coordinate system. The microphone of 0° is at a downstream position with coordinates of $(x, y, z) = (50, 0, 0)$.

The SPLs of the total noise, p'_{total} , and its components, p'_T , p'_{L1} , and p'_{L2} , at the microphones of 60° , 90° , and 120° are shown in Fig. 21. At $Re = 1000$, an energy bulge appears first around $St = 0.2$. The second bulge between 3 and 9 is not obvious at the downstream microphone of 60° . p'_T is always the largest part. p'_{L1} is higher than p'_{L2} at very low St that is below 0.03 at 60° and below 0.1 at 120° . At the rest of St , p'_{L1} is smaller than p'_{L2} . Similar phenomena are found at $Re = 5000$ although the characteristic frequencies are changed.

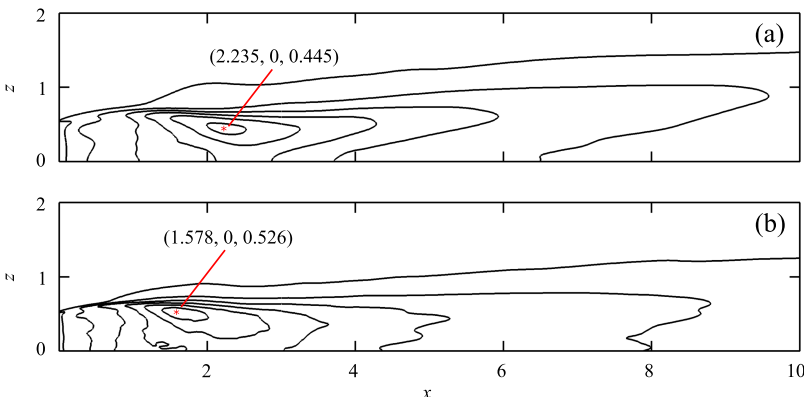


FIG. 19. Contours of u'_{rms}/U_0 in the cut plane of $y = 0$ at (a) $Re = 1000$ and (b) $Re = 5000$. The contour levels are 0.02, 0.064, 0.108, 0.152, 0.196, and 0.24. The red asterisks mark the locations of the highest values, which are 0.254 and 0.261 in the former and latter cases, respectively.

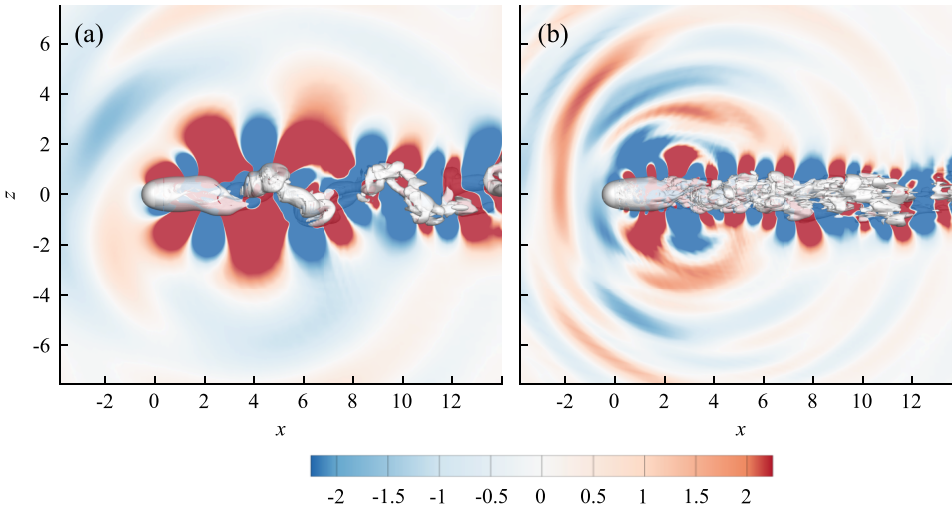


FIG. 20. Snapshots of the pressure fluctuations in the cut plane of $y = 0$ at (a) $Re = 1000$ and (b) $Re = 5000$. The white 3D isosurfaces viewed from the side are drawn for the dimensionless vorticity magnitude, $|\omega|D/U_0 = 0.8$.

Two bulges are clearly observed. St of the first bulge is around 0.25. The second bulge exists between approximately $St = 8$ and 13. The bound St , at which p'_{L1} and p'_{L2} switch their contributions to the total noise, is 0.07 at 60° and 0.1 at 120° . At 90° , the two noise components have similar contributions for $St < 0.1$.

Overall sound pressure levels (OASPLs) of p'_{total} and its components, p'_T , p'_{L1} , and p'_{L2} , are shown in Fig. 22. The contributions of the components are in line with the observations in the SPLs. A monopole directivity is a feature of p'_T , whereas

dipole directivities are features of p'_{L1} and p'_{L2} . The poles of p'_{L1} distribute horizontally and those of p'_{L2} vertically. Moreover, the downstream OASPL of p'_{total} is larger than the upstream OASPL. This result indicates that the noise is mainly emitted from the wake.

Due to the Doppler effect, the radiation distance from a source at \vec{y} to a microphone at \vec{x} is formulated as

$$R^* = |\vec{x} - \vec{y}| = |\vec{x}| \left[1 - \frac{\vec{x} \cdot \vec{y}}{|\vec{x}|^2} + O\left(\frac{|\vec{y}|^2}{|\vec{x}|^2}\right) \right], \quad (15)$$

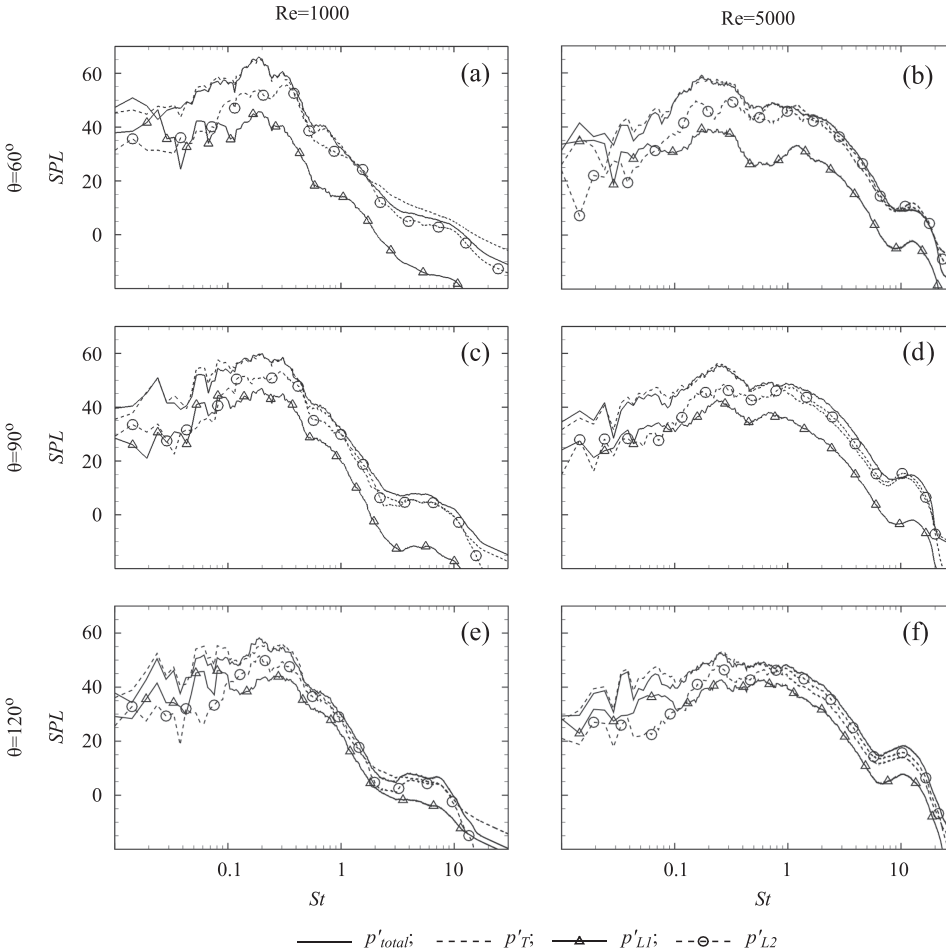


FIG. 21. The SPLs of the total noise, p'_{total} , and its components, p'_T , p'_{L1} , and p'_{L2} , computed for the microphones at θ of 60° at (a) $Re = 1000$ and (b) $Re = 5000$, 90° at (c) $Re = 1000$ and (d) $Re = 5000$, and 120° at (e) $Re = 1000$ and (f) $Re = 5000$.

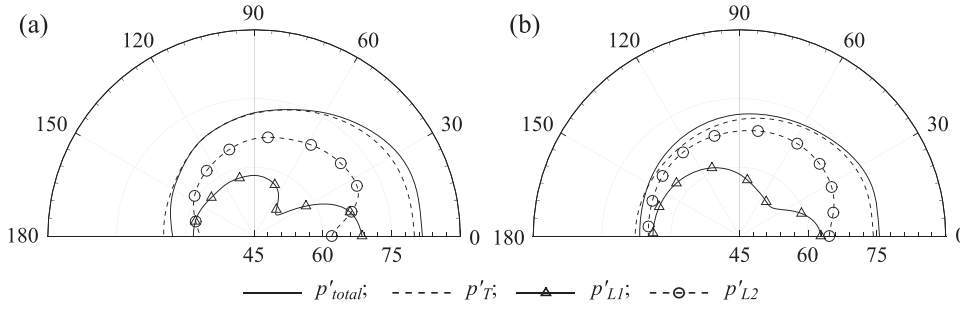


FIG. 22. The OASPLs of the total noise p'_{total} and its components, p'_T , p'_{L1} , and p'_{L2} , at (a) $Re = 1000$ and (b) $Re = 5000$.

and the position vectors, \vec{x} and \vec{y} , are written as

$$\begin{aligned}\vec{x} &= (\tilde{x}_1, \tilde{x}_2, \tilde{x}_3) = (x_1, \beta x_2, \beta x_3), \\ \vec{y} &= (\tilde{y}_1, \tilde{y}_2, \tilde{y}_3) = (y_1, \beta y_2, \beta y_3),\end{aligned}\quad (16)$$

where $\beta = \sqrt{1 - (U_0/c_0)^2}$. If $\vec{x} \gg \vec{y}$, then a far-field microphone position can be defined by neglecting the last term in Eq. (15).²⁷ For a quantitative estimation, a far-field microphone position is regarded to satisfy the condition of $|\vec{x}| > 10L$ in a flow at a low Mach number of Ma_0 , where L is the characteristic length of a flow structure. As the flow structure is swept downstream, the characteristic length at the frequency f is approximated as $L \sim Ma_0 c_0 / f$. The frequency in the far field is therefore given by $f > 10Ma_0 c_0 / |\vec{x}|$. A further approximation is given by $|\vec{x}| \approx |\vec{r}|$ due to $\beta \approx 1$ in the low Mach number flow. Regarding $|\vec{x}| = 50$ and $Ma_0 = 0.294$ in the present study, a far-field frequency is larger than 20 Hz. In the computation of the OASPLs, the frequency range of 1 Hz–3000 Hz is taken into account so that near-field frequencies are included. This computation is still valid since the approximation in Eq. (15) is not used in the acoustics formulations described in the Appendix.

The SPLs of p'_{total} and p'_{wall} , which are the noise generated by the fluctuating pressure on the walls, at the microphones of 30° and 150° are displayed in Fig. 23. p'_{wall} is negligible in comparison with p'_{total} . This effect is more obvious at the downstream microphone of 30° . At low St below 0.3, the high Re case has smaller p'_{total} and p'_{wall} than the low Re case. However, the noise at high frequencies in the high Re case is noticeably high. It suggests that the turbulence in the wake plays a dominant role in the noise generation, whereas the coherent structures become a weaker contributor to the noise.

The ratio of p'_{wall} to p'_{total} is defined as

$$r_{wall} = \frac{\sum_{i=n_c}^{N_c} \hat{E}_{wall}(f_i)}{\sum_{i=n_c}^{N_c} \hat{E}_{total}(f_i)}, \quad (17)$$

where $\hat{E}(f_i) = |\hat{p}'(f_i)|^2$ and n_c and N_c are the lowest and highest indices of discrete frequencies, respectively. The ratio r_{wall} , which is computed with $f_{nc} = 1$ Hz and $f_{Nc} = 3000$ Hz, is shown in Fig. 24. It is observed that r_{wall} is less than 0.006 at $Re = 1000$ and 0.02 at $Re = 5000$. These small values quantify the noise from the surface pressure, which is in the form of dipole sources. Moreover, the largest ratio appears at the upstream microphone at 180° in both the cases. The ratios at the downstream microphones in the low Re case approach zero, while those in the high Re case are detected with small magnitudes below 0.002. The negligible ratios indicate that the noise from the wakes is predominant as compared with that from the pressure on the walls. In the flows studied in this work, the volume noise sources that are in the form of quadrupoles are more important than the surface noise sources that behave as dipoles.

In the present hemisphere flows, the thickness noise term from the permeable surface, p'_T , is predominant in comparison with the loading noise terms from the same surface, p'_{L1} and p'_{L2} , as shown in Figs. 21 and 22. The contribution of the loading noise from the wall pressure, p'_{wall} , to the total noise is very limited, as displayed in Fig. 24. However, these observations are different from the findings in flows past a circular cylinder,^{28–30} where the loading noise showing a dipole pattern is predominant. These differences can be explained based on the formation and location of the powerful noise sources. In the cylinder flows, the vortex shedding near the surface is regarded as the major noise sources.³¹ Moreover,

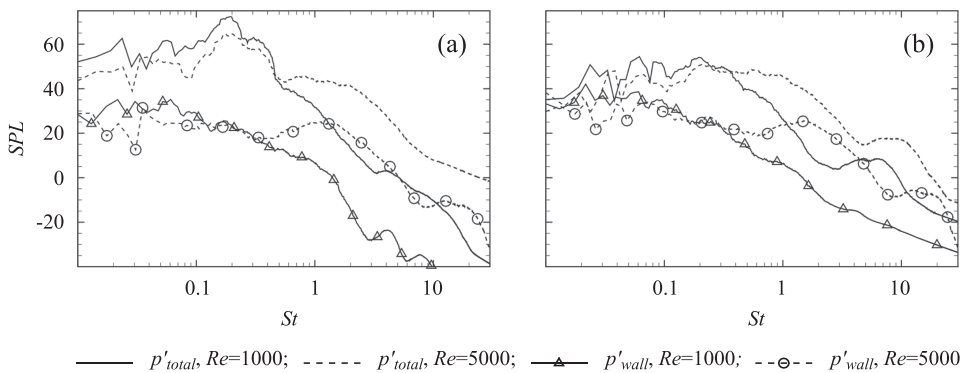
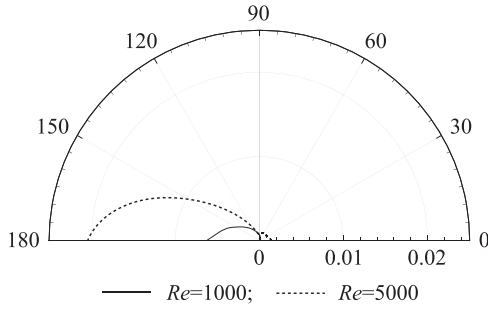


FIG. 23. The SPLs of p'_{total} and p'_{wall} at the two Re computed for the microphones of (a) 30° and (b) 150° .

FIG. 24. r_{wall} at different Re .

Cheong *et al.*³² found that the cylinder surface downstream the flow separation confines the shedding development so that intensive hydrodynamic pressure fluctuations are observed at the angles of $45^\circ < \theta < 100^\circ$ and $260^\circ < \theta < 315^\circ$. They put forward that the wall confinement results in the shear-noise sources, $\partial^2 [\rho (u'_i \bar{u}_j + \rho \bar{u}_i u'_j)] / \partial x_i \partial x_j$, dominating the noise generation. Since these sources are located near the surface, the noise from them is effectively scattered by the surface.³³ In the hemisphere flows, only the high Re case presents the flow separation with a short distance, approximately 0.02 m, upstream the hemisphere edge as illustrated in Figs. 13 and 14. The geometry back face, which is normal to the streamwise direction, exerts limited confinement to the shedding development. Energetic noise sources are not formed in the region of the shedding but near the end of the recirculation bubble. These sources are located at a distance of 2.2 away from the hemisphere surface in the low Re case and at 1.6 in the high Re case, as shown in Fig. 19. By means of visualizing the pressure fluctuations in Fig. 20, it is observed that significant noise is emitted from the wakes. In addition, due to the large distances, the scattering effect caused by the surface is reduced. It is found in Figs. 23 and 24 that the noise component from the fluctuating wall pressure is negligible.

VII. CONCLUSIONS

The noise from flows past a hemisphere is studied at $Re = 1000$ and $Re = 5000$. The boundary layers are laminar in the cases. Flow separation is observed in the latter case. The wake at low Re contains significant large scale coherent structures that are not axisymmetric and dissipate slowly. At high Re , a large amount of small scale turbulent vortices arise in the wake while the large structures diminish. Furthermore, the coefficients of the drag and lift components are turbulent in both the cases.

Since the wake becomes highly turbulent when Re increases, the energy reflected by u'_{rms} decays fast in the streamwise direction. The high energy region moves upstream. Moreover, the mean drag decreases. In the spectra of the drag and lift components, it is found that the increase of high frequency energy accompanies the decrease of low frequency energy. This finding is consistent with the transformation of the flow structures in the wakes.

The important noise sources are found in the wakes in both the cases. At high Re , the predominant source region is recognized at the end of the recirculation bubble, where the convection is significant. In addition, two energy bulges are

identified in the noise spectra in both the cases. At low Re , the first bulge frequency is approximately $St = 0.2$, and the second one is in the range of $St = 3-9$. At high Re , the first bulge frequency is approximately 0.25. The second bulge is observed for $8 < St < 13$.

The noise from the flows is analyzed according to its components formulated in formulation 1C of the FW-H method. The components are p'_T , $p'_{L,1}$, and $p'_{L,2}$ associated with mass flux, momentum flux, and pressure. In the spectra, p'_T is the predominant component. The loading noise component, $p'_{L,1}$, is higher than the other one, $p'_{L,2}$, at low frequencies for the far-field microphones at 60° and 120° , while they are similar at 90° . However, $p'_{L,2}$ generally exceeds $p'_{L,1}$ at high frequencies. Furthermore, a monopole pattern is identified in p'_T . A streamwise dipole pattern is found in $p'_{L,1}$ and a transverse dipole pattern in $p'_{L,2}$.

The wakes are the predominant noise contributors as compared with the pressure on the walls. The quadrupole volume sources are therefore more important than the dipole surface sources in the flows concerned in this work.

A buffer surface is set up in the downstream end of the permeable integral surface to compensate the artificial noise caused by the cutoff quantities.^{17,24-26} This buffer surface can be specified based on the buffer zone that is used to damp the quantities in the flow computation. Validation of the correction method is carried out. It is found that the buffer surface effectively eliminates the numerical contamination at low frequencies for the present flows.

ACKNOWLEDGMENTS

The authors appreciate the Swedish National Infrastructure for Computing (SNIC) for providing computer resources.

APPENDIX: F1C OF FW-H ACOUSTIC ANALOGY

The FW-H acoustic analogy, F1C, takes into account the ambient medium moving with a uniform speed. By introducing the step Heaviside function into the Navier-Stokes equations and manipulating the equation terms, F1C is formulated as^{9,10}

$$\square^2 p'(\vec{x}, t) = \left(\frac{\partial}{\partial t} + U_{0j} \frac{\partial}{\partial x_j} \right) [Q_k n_k \delta(f)] - \frac{\partial}{\partial x_i} [L_{ij} n_j \delta(f)] + \frac{\partial^2}{\partial x_i \partial x_j} [\bar{T}_{ij} H(f)], \quad (A1)$$

with the wave operator on the left hand side given by

$$\square^2 = \frac{\partial^2}{\partial t^2} - c_0^2 \frac{\partial^2}{\partial x_j^2} + 2U_{0j} \frac{\partial^2}{\partial t \partial x_j} + U_{0i} U_{0j} \frac{\partial^2}{\partial x_i \partial x_j}, \quad (A2)$$

where c_0 denotes the speed of sound in the ambient medium and U_{0i} denotes the medium moving velocity vector. $f(\vec{x}) = 0$ represents the control surface, where the Heaviside function is applied. n_i denotes unit vectors that are outward normal to the control surface. δ is the Dirac delta function. The bar on T_{ij} signifies the generalized derivatives.⁸ The source term, Q_j , is

$$Q_j = \rho (u_j + U_{0j} - v_j) + \rho_0 (v_j - U_{0j}). \quad (A3)$$

The term, L_{ij} , is

$$L_{ij} = F_{ij} + P_{ij} \quad (\text{A4})$$

with

$$F_{ij} = \rho u_i (u_j + U_{0j} - v_j), \quad (\text{A5a})$$

$$P_{ij} = (p - p_0) \delta_{ij} - \sigma_{ij}, \quad (\text{A5b})$$

where v_j is a velocity component of the control surface. T_{ij} is the Lighthill stress tensor formulated as

$$T_{ij} = (p' - \rho' c_0^2) \delta_{ij} - \tau_{ij} + \rho u_i u_j, \quad (\text{A6})$$

where δ_{ij} is the Kronecker delta.

The source terms relate to variations of the mass flow, momentum, pressure, and the Lighthill stress tensors. The mean flow velocity can be aligned along the x_1 axis. Using Green's function in free space, the solution of Eq. (A1) includes the following components:¹⁰

$$4\pi p'_T = \frac{\partial}{\partial t} \int_{f=0} \left[\frac{Q_j n_j}{R^* (1 - M_R)} \right]_{ret} dS - M_0 \frac{\partial}{\partial t} \int_{f=0} \left[\frac{\tilde{R}_1 Q_j n_j}{R^* (1 - M_R)} \right]_{ret} dS - U_0 \int_{f=0} \left[\frac{\tilde{R}_1^* Q_j n_j}{R^{*2} (1 - M_R)} \right]_{ret} dS, \quad (\text{A7a})$$

$$4\pi p'_{L1} = \frac{1}{c_0} \frac{\partial}{\partial t} \int_{f=0} \left[\frac{F_{ij} n_j \tilde{R}_i}{R^* (1 - M_R)} \right]_{ret} dS + \frac{\partial}{\partial t} \int_{f=0} \left[\frac{F_{ij} n_j \tilde{R}_i^*}{R^{*2} (1 - M_R)} \right]_{ret} dS, \quad (\text{A7b})$$

$$4\pi p'_{L2} = \frac{1}{c_0} \frac{\partial}{\partial t} \int_{f=0} \left[\frac{P_{ij} n_j \tilde{R}_i}{R^* (1 - M_R)} \right]_{ret} dS + \frac{\partial}{\partial t} \int_{f=0} \left[\frac{P_{ij} n_j \tilde{R}_i^*}{R^{*2} (1 - M_R)} \right]_{ret} dS, \quad (\text{A7c})$$

$$4\pi p'_V = \frac{\partial^2}{\partial x_i \partial x_j} \int_{f>0} \left[\frac{T_{ij}}{R^* (1 - M_R)} \right]_{ret} dV. \quad (\text{A7d})$$

Here, the variables in Eq. (A7) are defined as follows:

$$R = \frac{-M_0 (x_1 - y_1) + R^*}{\beta^2}, \quad (\text{A8a})$$

$$R^* = \sqrt{(x_1 - y_1)^2 + \beta^2 [(x_2 - y_2)^2 + (x_3 - y_3)^2]}, \quad (\text{A8b})$$

$$\beta = \sqrt{1 - M_0^2}, \quad (\text{A8c})$$

$$\tilde{R}_1 = \frac{1}{\beta^2} (-M_0 + \tilde{R}_1^*), \quad (\text{A8d})$$

$$\tilde{R}_2 = \frac{x_2 - y_2}{R^*}, \quad (\text{A8e})$$

$$\tilde{R}_3 = \frac{x_3 - y_3}{R^*}, \quad (\text{A8f})$$

$$\tilde{R}_1^* = \frac{x_1 - y_1}{R^*}, \quad (\text{A8g})$$

$$\tilde{R}_2^* = \beta \frac{x_2 - y_2}{R^*}, \quad (\text{A8h})$$

$$\tilde{R}_3^* = \beta \frac{x_3 - y_3}{R^*}, \quad (\text{A8i})$$

$$M_R = \frac{1}{c_0} v_i \tilde{R}_i. \quad (\text{A8j})$$

The terms with subscript “ret” are formulated at the retarded time, $\tau = t - R/c_0$. R is the refracted acoustic distance between an observer and a source point. The refraction is caused by the convection effect of the moving ambient medium.^{9,10}

It is worth noting that if the control surface lies on the rigid walls, p'_T relates to the thickness noise, the sum of p'_{L1} and p'_{L2} to the loading noise, and p'_V to the quadrupole noise. However, these physical meanings are not retained if the control surface is permeable. In this situation, p'_T , p'_{L1} , and p'_{L2} result from variations of the mass flux ρu_i , the momentum flux $\rho u_i u_j$, and the pressure p , respectively. The method of employing the permeable surface brings the benefit that p'_V can be neglected. There is therefore great savings in the computational resources. This method is used in this work.

¹D. Kim and H. Choi, “Laminar flow past a hemisphere,” *Phys. Fluids* **15**(8), 2457–2460 (2003).

²M. J. Lighthill, “On sound generated aerodynamically. I. General theory,” *Proc. R. Soc. A* **211**, 564–587 (1952).

³M. J. Lighthill, “On sound generated aerodynamically. II. Turbulence as a source of sound,” *Proc. R. Soc. A* **222**, 1–32 (1954).

⁴N. Curle, “The influence of solid boundaries upon aerodynamic sound,” *Proc. R. Soc. A* **231**, 505–514 (1955).

⁵J. E. F. Williams and D. L. Hawkings, “Sound generation by turbulence and surfaces in arbitrary motion,” *Philos. Trans. R. Soc., A* **264**, 321–342 (1969).

⁶F. Farassat, “Derivation of Formulations 1 and 1A of Farassat,” NASA/TM-2007-214853 (2007).

⁷K. S. Brentner and F. Farassat, “An analytical comparison of the acoustic analogy and Kirchhoff formulation for moving surfaces,” *AIAA J.* **36**, 1379–1386 (1998).

⁸K. S. Brentner and F. Farassat, “Modeling aerodynamically generated sound of helicopter rotors,” *Prog. Aerosp. Sci.* **39**, 83–120 (2003).

⁹V. L. Wells and A. Y. Han, “Acoustics of a moving source in a moving medium with application to propeller noise,” *J. Sound Vib.* **184**, 651–663 (1995).

¹⁰A. Najafi-Yazdi, G. A. Brès, and L. Mongeau, “An acoustic analogy formulation for moving sources in uniformly moving media,” *Proc. R. Soc. A* **467**, 144–165 (2011).

¹¹R. R. Mankbadi, M. H. Hayder, and L. Povinelli, “Structure of supersonic jet flow and its radiated sound,” *AIAA J.* **32**(5), 897–906 (1994).

¹²M. L. Shur, P. R. Spalart, M. Strelets, and A. K. Travin, “Towards the prediction of noise from jet engines,” *Int. J. Heat Fluid Flow* **24**, 551–561 (2003).

¹³M. Wang, S. K. Lele, and P. Moin, “Computation of quadrupole noise using acoustic analogy,” *AIAA J.* **34**(11), 2247–2254 (1996).

¹⁴D. P. Lockard and J. H. Casper, “Permeable surface corrections for Ffowcs Williams and Hawkings integrals,” AIAA Paper No. 2005–2995, 2005.

¹⁵H. D. Yao, L. E. Eriksson, L. Davidson, O. Grundestam, S. H. Peng, and P. E. Eliasson, “Aeroacoustic assessment of conceptual low-noise high-lift wing configurations,” AIAA Paper No. 2012–383, 2012.

¹⁶H.-D. Yao, L. Davidson, L.-E. Eriksson, O. Grundestam, S. H. Peng, and P. E. Eliasson, “Surface integral analogy approaches for predicting noise from 3d high-lift low-noise wings,” *Acta Mech. Sin.* **30**, 326–338 (2014).

¹⁷J. B. Freund, S. K. Lele, and P. Moin, “Calculation of the radiated sound field using an opening Kirchhoff surface,” *AIAA J.* **34**, 909–916 (1996).

¹⁸G. Erlebacher, M. Y. Hussaini, C. G. Speziale, and T. A. Zang, “Toward the large-eddy simulation of compressible turbulent flows,” *J. Fluid Mech.* **238**(1), 155–185 (1992).

¹⁹H. Mårtensson, L.-E. Eriksson, and P. Albråten, “Numerical simulations of unsteady wakeflow,” in International Symposium on Air Breathing, 9370–309, 1991.

²⁰L.-E. Eriksson, “Development and validation of highly modular flow solver versions in G2DFLOW and G3DFLOW,” Internal Report No. 9970-1162, Volvo Aero Corporation, Sweden, 1995.

- ²¹C. Wollblad, L.-E. Eriksson, and L. Davidson, "Semi-implicit preconditioning for wall-bounded flow," AIAA Paper No. 2004-2135, 2004.
- ²²T. Colonius, S. K. Lele, and P. Moin, "Boundary conditions for direct computation of aerodynamic sound generation," *AIAA J.* **31**, 1574-1582 (1993).
- ²³*Large-Eddy Simulation for Acoustics*, edited by C. Wagner, T. Hüttl, and P. Sagaut (Cambridge University, 2007).
- ²⁴T. Colonius, S. K. Lele, and P. Moin, "Sound generation in a mixing layer," *J. Fluid Mech.* **330**, 375-409 (1997).
- ²⁵L. Cheung and S. K. Lele, "Evaluation of far-field sound with open surface corrections to Lighthill's equation," AIAA Paper No. 2006-2488, 2006.
- ²⁶C. Bogey and C. Bailly, "Three-dimensional non-reflective boundary conditions for acoustic simulations: Far field formulation and validation test cases," *Acta Acust. Acust.* **88**, 463-471 (2002).
- ²⁷*Aeroacoustics*, edited by M. E. Goldstein (McGraw-Hill Book Company, New York, 1976).
- ²⁸F. Pérot, J. Auger, and H. Giardi, "Computation of the noise generated by low Mach number flows around a cylinder and a wall-mounted half-cylinder," AIAA Paper No. 2004-2859, 2004.
- ²⁹R. M. Orselli, J. R. Meneghini, and F. Saltra, "Two and three-dimensional simulation of sound generated by flow around a circular cylinder," AIAA Paper No. 2009-3270, 2009.
- ³⁰L. Guo, X. Zhang, and G. He, "Large-eddy simulation of circular cylinder flow at subcritical Reynolds number: Turbulent wake and sound radiation," *Acta Mech. Sin.* **32**, 1-11 (2016).
- ³¹*Acoustics of Fluid-Structure Interactions*, edited by M. S. Howe (Cambridge University, 2010).
- ³²C. Cheong, P. Joseph, Y. Park, and S. Lee, "Computation of aeolian tone from a circular cylinder using source models," *Appl. Acoust.* **69**, 110-126 (2008).
- ³³X. Gloerfelt, F. Pérot, C. Bailly, and D. Juvé, "Flow-induced cylinder noise formulated as a diffraction problem for low mach numbers," *J. Sound Vib.* **287**, 129-151 (2005).